Optics Communications 311 (2013) 163–171

Contents lists available at ScienceDirect

Optics Communications

journal homepage: www.elsevier.com/locate/optcom

Error reduction method for singularity point detection using Shack–Hartmann wavefront sensor

Chenxi Huang [a,1], Heye Zhang [b,1], Hongxin Huang [c], Haruyoshi Toyoda [c], Takashi Inoue [c], Huafeng Liu [a,*]

[a] State Key Laboratory of Modern Optical Instrumentation, Zhejiang University, Hangzhou, Zhejiang 310027, China
[b] Key Lab for Health Informatics of the Chinese Academy of Sciences, Institute of Biomedical and Health Engineering Shenzhen Advanced Institutes of Technology, Chinese Academic of Sciences, Shenzhen, China
[c] Central Research Laboratory, Hamamatsu Photonics K.K., 5000 Hirakuchi, Hamakita-ku, Hamamatsu, Shizuoka 434-8601, Japan

ARTICLE INFO

Article history:
Received 28 May 2013
Received in revised form
23 July 2013
Accepted 8 August 2013
Available online 30 August 2013

Keywords:
Shack–Hartmann wavefront sensor
Optical vortex
Phase singularities
Hybrid centroiding method

ABSTRACT

A new framework is proposed for realizing high-spatial-resolution detection of singularity points in optical vortex beams using a Shack–Hartmann wavefront sensor (SHWS). The method uses a Shack–Hartmann wavefront sensor (SHWS) to record a Hartmanngram. A map of evaluation values related to phase slope is then calculated from the Hartmanngram. We first determined the singularity's position precisely by calculating the centroid of the circulation of 3×3 crosspoints. After that, we analyzed the error distribution of it, and proposed hybrid centroiding framework for reducing its error. Optical experiments were carried out to verify the method. Good linearity was showed in detecting positions of the singularity points, and it was indicated that the accuracy of detection the position of OV was improved. The average root mean square (RMS) error over various measurements was better than correlation matching method, which we proposed before. The method not only shows higher accuracy, but also consumes much less time than our former work.

1. Introduction

Optical vortex (OV) beams [1–4] which are special optical fields having spiral phase structures around zero-amplitude points have found many applications, such as information encoding for quantum commnuications [5], trapping and rotating of micro-particles [6], stimulated emission depletion microscopy [7], and biological kinematic analysis [8]. The points of zero amplitude are typically lines in three-dimensional space and their intersections with a plane are typically isolated points [9]. The phase has spiral structures with continuously changing from 0 to $2n\pi$ (n is an integer and known as topological charge) around such points. The study of behaviors of OV has grown up to a sub-field of optical research, now known as singular optics.

One of the problems in singular optics is how to measure the spiral phase structures. This problem was addressed by interferometry [10,11] over the years. The principal advantage of interferometry is that its spatial resolution is high. However, it requires relatively complicated optics, and when vibrations exist, the measurement accuracy decreases significantly. Recently, some methods employing Shack–Hartmann wavefront sensors (SHWSs) [12,13] have been proposed to overcome these issues. A SHWS simply consists of a lenslet array and an image sensor at its back-focal plane, and measure directly the phase slope of incoming optical wave at each lenslet position. Therefore, a map of phase slope distribution can be easily obtained.

The fundamental basis of OV detection using SHWS is that the closed-line integral/contour sum of phase-slope-vector measured is non-zero if there is a net topological charge of a phase singularity within the area enclosed by the closed-line path. Because the smallest contour is the path connecting the neighboring lenslets, therefore, position determined with the contour-sum method has uncertainity corresponding to spacing of the lenslet. Growing out of the contour sum method, some new solutions have been proposed to achieve more robust results against noise [9,14,15]. An alternative approach, where singularities are determined from phase slope vector data based on the branch point potential method [16,17], has been introduced. We also proposed a correlation matching method for improving the spatial accuracy of position measurement [18]. This method requires a set of references obtained by numerical calculation. It requires relatively long computing time because the matching operation must be done between the circulation obtained from real Hartmanngram and the references.

In this paper, we propose a hybrid centroiding framework which detects OV with the aid of two centroiding methods, which

* Corresponding author.
E-mail address: huafeng@ieee.org (H. Liu).
[1] These authors contribute equally to this work and they share the first authorship.

0030-4018/$ - see front matter © 2013 Elsevier B.V. All rights reserved.
http://dx.doi.org/10.1016/j.optcom.2013.08.019

identify the center of gravity. In the following, we propose a 9-Points Centroiding method for measuring OV position and analyze its error distribution in Section 2, and then a hybrid centroiding framework to reduce the error is presented in Section 3. In Section 4, optical experiments was carried, and good linearity was shown. Finally, we summarize our work in Section 5.

2. 9PCM (9-Points Centroiding method) and its Numerical Analysis of Error Distribution

We resolve our new method, the 9PCM (9-Points Centroiding method) in the rest of this paper, into two stages. A circulation map that represents phase structure is, firstly, calculated from an image acquired with an SHWS, which is call Hartmanngram, by using the conventional contour sum method, by which phase singularities are roughly determined from the map. After that, the position of each phase singularity point is determined more accurately by the hybrid centroiding step.

2.1. Circulation map calculation step to locate an optical vortex with lens-size precision

Around the singularity point, the phase changes continuously from 0 to $2n\pi$. An optical vortex, therefore, can be detected with the aid of a closed line integral [19],

$$\int_C \nabla\theta d\vec{l} = 2\pi n, \tag{1}$$

where C is the closed integration contour, $\nabla\theta$ denotes the gradient of the phase distribution, which represents a two-dimensional distribution of phase slope vector, $d\vec{l}$ is the element of the contour, and n is an integer that represents the net topological charge of a phase singularity within the area enclosed by the contour.

A beam is divided into multiple sub-beams by the lenslet array of SHWS, when the beam is incident on it. The SHWS acquires an image, which is called a Hartmanngram, consisting of many bright spots formed by sub-beams. The position of the bright spot formed by a sub-beam deviates from the center of the lenslet that creates that sub-beam, when the wavefront of the sub-beam tilts, and the amount of movement of the bright spot is proportional to the tilting angle of the sub-beam. We can calculate the phase slope vector, therefore, from the positions of the spots. A discrete version of the phase-slope-vector distribution can be obtained, by calculating phase slope at each lenslet.

Eq. (1) has to be modified into a discrete version, by which the equivalent of it from the discrete phase-slope-vector distribution can be calculated. Such modification is represented in Fig. 1. We calculate a phase slope vector $(S_x^{i,j}, S_y^{i,j})$ at lenslet (i, j). The dashed lines in Fig. 1 represent a closed contour, which has a rectangular shape, and can be formed by connecting the centers of four neighboring lenslets. The four neighboring lenslets have a common point, as shown in Fig. 1, which is also the center of the rectangle contour. This common point is referred to as a crosspoint (p, q). The closed line integral can be equivalently written as [19],

$$Cir\ (p,\ q) = \frac{w}{2}(S_x^{i,j} + S_x^{i,j+1} + S_y^{i,j+1} + S_y^{i+1,j+1} - S_x^{i+1,j+1} - S_x^{i+1,j} - S_y^{i+1,j} - S_y^{i,j}), \tag{2}$$

where w is the lens size of the lenslet array and $Cir(p, q)$ is called the circulation at crosspoint (p, q). A circulation map can be obtained by calculating the circulation at every crosspoint.

$Cir(p, q)$ is similar to but not identical to the close-line integral calculated by Eq. (1), as it is a discrete approximation. Let us consider the case when no singularity point is present within the contour area around (p, q) and there is no singularity in the other areas. When no singularity exists in the area, $Cir(p, q)$ approaches zero. $Cir(p, q)$ becomes non-zero in the case when one singularity exists. Not only that, the circulations at the eight nearest crosspoints to the crosspoint (p, q) tend to have non-zero values. However, previous studies shows that $Cir(p, q)$ is the largest among such non-zero values [19]. By finding the local maximum in the circulation map, we can locate the nearest crosspoint to a singularity point, which can be expressed as:

$$(p_{max},\ q_{max}) = \mathrm{maxpos}(Cir(p,\ q)), \tag{3}$$

where maxpos() denotes an operation of searching for a local maximum and returning its position, and (p_{max}, q_{max}) represents the crosspoint position. At present, the position of the singularity point has an uncertainty corresponding to the lenslet size. In other words, the maximum error of the position of the singular point is half of the lenslet size.

2.2. 9-Points centroiding step to achieve precise location

In the next step, we attempt to determine a more accurate position of the singularity point. While the singularity point is specified as being in the contour area of Crosspoint (p, q) in the

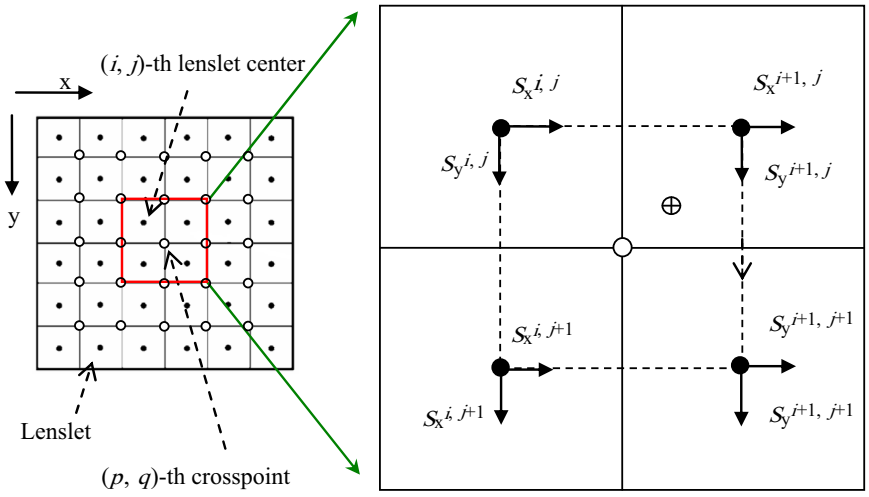

Fig. 1. Concept of circulation. S*x* and S*y* represents phase slopes in *x*-axis (horizontal) and *y*-axis (vertical) directions, and *i*, *j* denotes the lenslet index. The solid circles are the centers of lenslets, and the open circles indicate crosspoints of neighboring 2×2 lenslets. The dashed line indicates a contour connecting the centers of the four neighboring lenslets. The symbol "⊕" denotes the position of phase singularity point.

first step, we choose nine circulations (3×3 crosspoints) around the crosspoint (p, q). We call the chosen 3×3 crosspoints a circulation submap. A model for a circulation submap is shown in Fig. 2, which includes 4×4 lenslets and 3×3 crosspoints. The solid circles and the open circles indicate the centers and the crosspoints of the lenslets, respectively. Also, u and v are the horizontal and vertical axes normalized by the lenslet size, respectively. The center crosspoint is taken as the origin of the u–v coordinate system O, and it is assumed that a phase singularity point is present at $(u_0, v_0)(-0.5<u_0\le0.5,\ -0.5<v_0\le0.5)$. The position of other 8 crosspoints in this coordinate system is denoted as (k, l), $(k, l=-1, 0, 1)$. The singularity point is, of course, the center of the spiral phase distribution and is denoted by a symbol "⊕". The accurate position of OV is calculated using our new method under these conditions.

In this method, the position of OV (u^{9PCM}, v^{9PCM}) measured by calculating centroiding of the 9 crosspoints, which can be expressed as

$$u^{9PCM}=\frac{\sum_{k=-1}^{1}\sum_{l=-1}^{1}C(k,\ l)k}{\sum_{k=-1}^{1}\sum_{l=-1}^{1}C(k,\ l)}$$

$$v^{9PCM}=\frac{\sum_{k=-1}^{1}\sum_{l=-1}^{1}C(k,\ l)l}{\sum_{k=-1}^{1}\sum_{l=-1}^{1}C(k,\ l)} \tag{4}$$

where $C(k,\ l)=Cir(p_{\max}+k,\ q_{\max}+l)$ $(k, l=-1, 0, 1)$, and k, l means relative locations in this coordinate system.

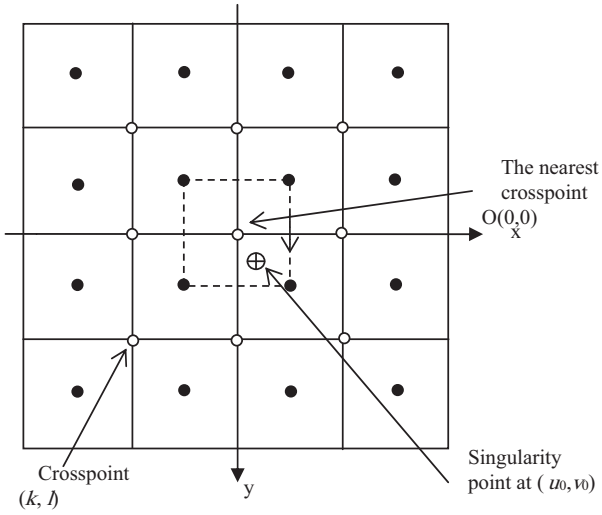

Fig. 2. A model for the circulation submap.

The position (P, Q) of the singularity, in high precision, can be expressed as

$$P=p_{\max}+u^{9PCM},$$
$$Q=q_{\max}+v^{9PCM}. \tag{4}$$

2.3. Numerical Analysis of Error Distribution for 9PCM

A numerical calculation was made to test the 9-Points Centroiding methods above. An OV, the position of which was set in advance, is simulated to emit on the SHWS. The circulations for the crosspoints near the OV can be calculated by the method we introduced above.

The position of OV was moved in the step of 0.01, individually, in horizontal and vertical direction in the region: $(-0.5<u_0\le0.5,\ -0.5<v_0\le0.5)$, where the circulation for each crosspoint $C(k, l)$ can be calculated by using Chen's method [19]. The 9PCM (Eq. (4)) and the 4PCM (Eq. (5)) are used, individually, to measure the position of the OV in each case. In each location, the error of the true position and the position calculated respectively by 9PCM and 4PCM, are calculated, which can be written as

$$Err^{9PCM}(u_0,\ v_0)=\sqrt{(u_0-u^{9PCM}_{u0,\ v0})^2+(v_0-v^{9PCM}_{u0,\ v0})^2} \tag{5}$$

where $u^{9PCM}_{u0,\ v0}$ and $v^{9PCM}_{u0,\ v0}$ mean the position calculated by the 9PCM in horizontal and vertical direction of OV. The distribution of $Err^{9PCM}(u_0,\ v_0)$ are shown in Fig. 4(a). The precise shapes of the function for error distribution as one dimensional functions of $r=\sqrt{u^2+v^2}$ are shown in Fig. 4(b) for $v=0$ (middle line) and for $u=v$ (diagonal). It is found that the error distribution showed symmetrical characteristic. The error was zero when OV just locates in the center, or the crosspoint. The error tends to be larger when OV locates farther from the center. When OV locates in the corner of the distribution, or the center of a lenslet, the error would tend to be the largest.

3. Hybrid centroiding framework for determination of vortex position

By the analysis we mentioned in Section 2.3, it is indicated that the error tends to be very large when OV locates near the center of a lenslet. It means that 9PCM may not be suitable for calculating the position of OV in this situation. Fig. 4(a) is similar to Fig. 2 except that the singularity point located near the center of a lenslet. The 3×3 crosspoints was labeled as O, A, B, C, …, H. Fig. 5 (b) is a circulation distribution as a function of (u, v),where the 9 crosspoints was tagged. It is clear that the circulation of all the nearest 4 crosspoints: O, A, B, C, which also form the 4 corners of a lenslet, larger than 2.5. And the other 5 crosspoints that locates far from the OV have a very small circulation. If we calculate the

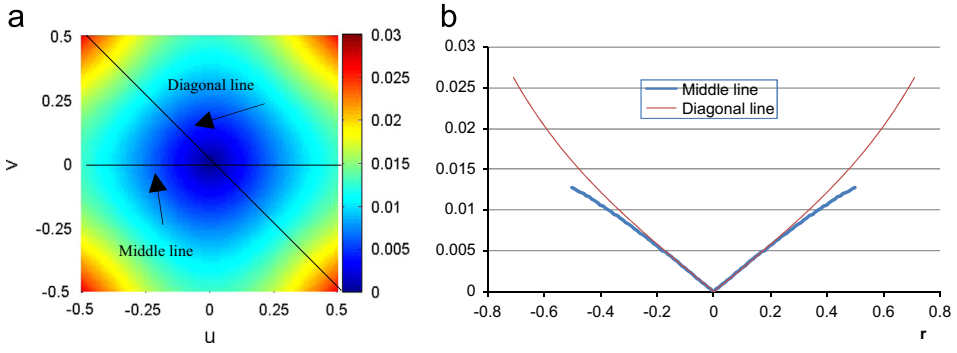

Fig. 3. (a) Error distribution of 9PCM and (b) one-dimensional functions of error distribution plotted as functions of $r=\sqrt{u^2+v^2}$ along the diagonal line and middle line, respectively, as indicated in (a). (For interpretation of the references to color in this figure, the reader is referred to the web version of this article)

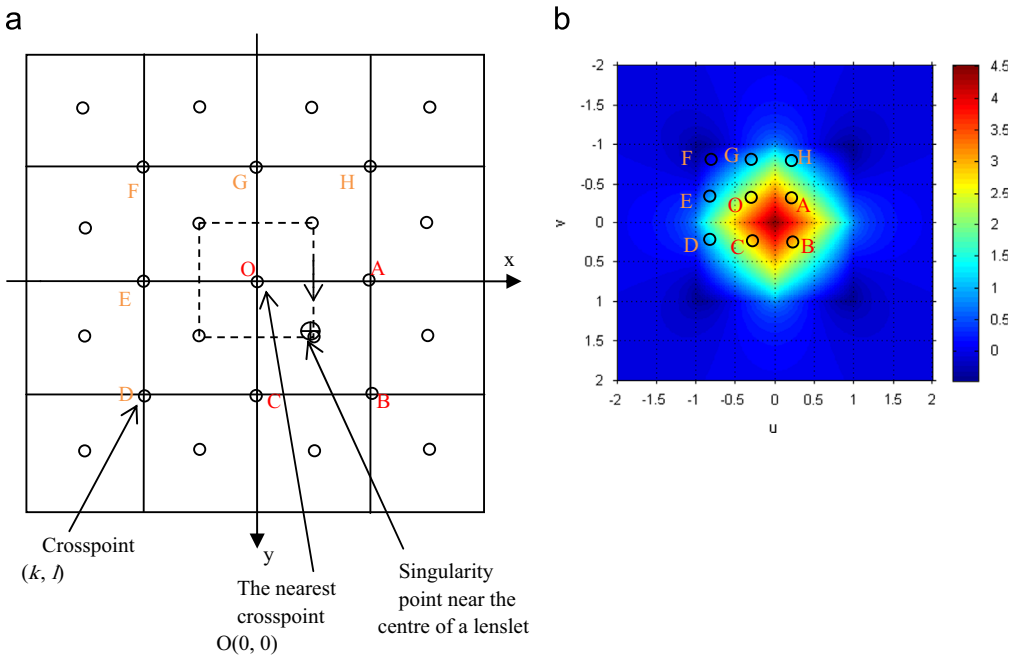

Fig. 4. (a) A model for the circulation submap in the case when singularity point locates near the center of a lenslet. (b) The circulation distribution as a function of (u, v).

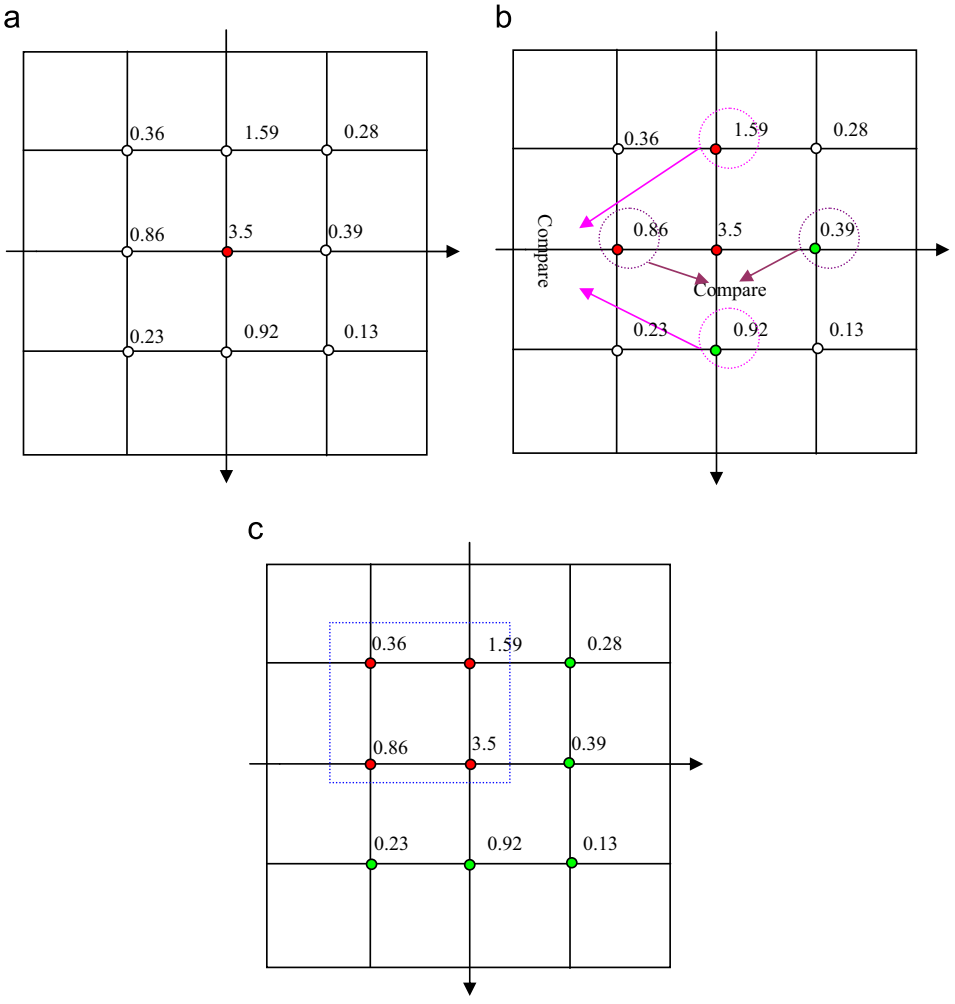

Fig. 5. An example for 4-Points method. Circles filled by white mean that $\omega_{k,l}$ $(k, l=-1, 0, 1)$ has not yet been determined in this step, the ones filled by red indicate $\omega_{k,l}=1$, and the ones filled by green indicate $\omega_{k,l}=0$. (For interpretation of the references to color in this figure legend, the reader is referred to the web version of this article.)

location of OV by only the circulation of the nearest 4 crosspoints in this situation, the error would fall down. We would introduce a 4-Points Centroiding method and combine it to our former framework in the next step.

3.1. 4-Points Centroiding method (4PCM)

We calculate the position of OV (u^{4PCM}, v^{4PCM}) by the following equation:

$$u^{4PCM}=\frac{\sum_{k=-1}^{1}\sum_{l=-1}^{1}C(k,\ l)k\omega_{k,\ l}}{\sum_{k=-1}^{1}\sum_{l=-1}^{1}C(k,\ l)\omega_{k,\ l}}$$
$$v^{4PCM}=\frac{\sum_{k=-1}^{1}\sum_{l=-1}^{1}C(k,\ l)l\omega_{k,\ l}}{\sum_{k=-1}^{1}\sum_{l=-1}^{1}C(k,\ l)\omega_{k,\ l}} \quad (6)$$

where $\omega_{k,\ l}$ denotes the weight at Crosspoint $C(k,\ l)$, which has only 2 values: 0 and 1. Four of them equal 1, the others equal 0. Fig. 3 shows how to determine the value of $\omega_{k,\ l}$. The 3×3 open circles denote the circulation submap, and the values above them show an example of the circulation for the crosspoint, respectively. Circles filled with white mean that $\omega_{k,\ l}$ has not yet been determined in this step, the ones filled with red indicate $\omega_{k,\ l}=1$, and the ones filled with green indicate $\omega_{k,\ l}=0$. The weight is determined by the following steps (shown in Fig. 3).

a) $\omega_{0,\ 0}=1$, as shown in Fig. 3(a).
b) As in Fig. 3(b), $\omega_{-1,\ 0}$ and $\omega_{1,\ 0}$ are determined by comparing of $C(-1,\ 0)$ and $C(1,\ 0)$.$\omega_{-1,\ 0}=1$, $\omega_{1,\ 0}=0$ can be concluded if the former one is bigger, and vice versa. $\omega_{-1,\ 0}$ and $\omega_{1,\ 0}$ can be determined in a similar way.
c) As in Fig. 3(c), the three points, whose weights equal 1 form three vertexes of a square and the fourth vertex tends to be the fourth point.

3.2. Hybrid centroiding method (HCM)

A numerical calculation similar to Section 2.3 was made to test the two centroiding methods above and verify our thought. In each location, the error of the true position and the position calculated respectively by 9PCM and 4PCM, are calculated, and the error are shown in Fig. 6(a) and (b). We can find out that they have different performance in different regions. The 9PCM shows a low error in most area except the area near the corner. The 4PCM, in contrast, shows better performance in the area near the corner. The map combines the regions where the error is lower in (a) and (b) is shown in (c), and its method distribution is shown in Fig. 6(d), where the boundaries of the two methods are clearly shown. As we have indicated before, the error in the whole map would fall down if we combine these two methods.

We focus on the criterion in determining which method is better for different situations, to restrain the error as low as possible. The boundary, of course, represents where the error by using 9PCM equals that by using 4PCM. In other words, we have to gain the curve of

$$uErr^{9PCM}_{u0,\ v0}=uErr^{4PCM}_{u0,\ v0} \quad (7)$$

The boundary in Fig. 4(d) can be, approximately, regarded as four linear equation, which can be can be written as

$$|u0|=k|v0|+b \quad (8)$$

Least square fitting was made, and the coefficient was calculated: $k=1.00$, $b=0.67$. The criterion for 9PCM can be written as

$$\begin{bmatrix}1 & k\\ 1 & -k\\ -1 & k\\ -1 & -k\end{bmatrix}\begin{bmatrix}u0\\ v0\end{bmatrix}\le b \quad (9)$$

When used in actual experiment, $u0$, $v0$ was replaced by estimated value $\hat{u}$, $\hat{v}$, and Eq. (9) can be written as

$$\begin{bmatrix}1 & k\\ 1 & -k\\ -1 & k\\ -1 & -k\end{bmatrix}\begin{bmatrix}\hat{u}\\ \hat{v}\end{bmatrix}\le b \quad (10)$$

In our method, the 9PCM was, firstly, used to calculate the accurate location of OV. Eq. (10) was used to determine which

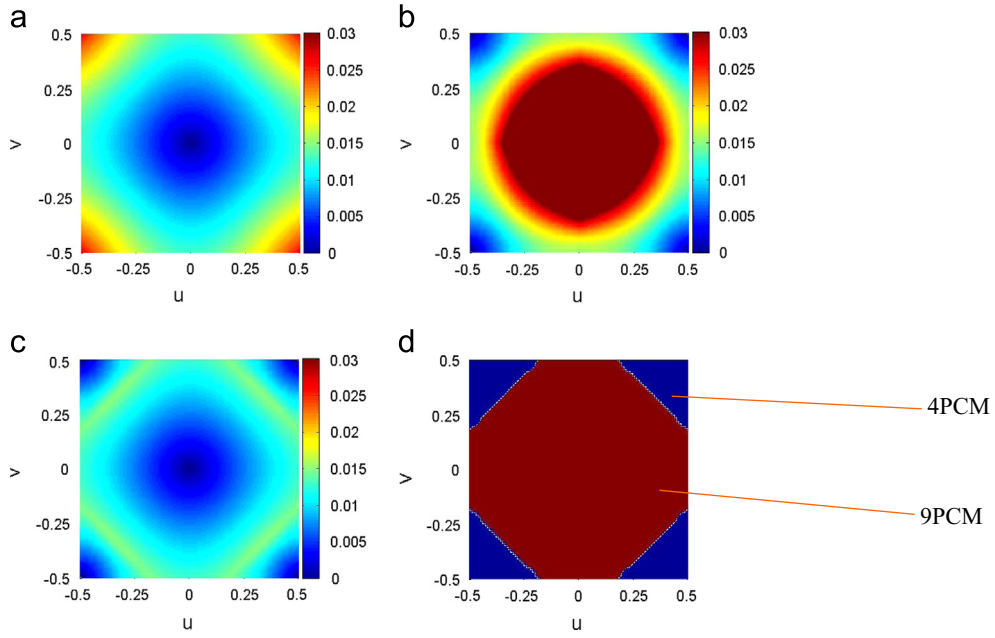

Fig. 6. The error distribution for the location of OV in horizontal direction for the 9PCM (a) and 4PCM (b), which were combined in (c). The distribution that shows lower error of the 9PCM and 4PCM is shown in (d).

method to choose, where $\hat{u}$, $\hat{v}$ was represented by u^{9PCM} and v^{9PCM}. It can be written as

$$u_{\max} = \begin{cases} u^{9PCM}, & \text{when Eq. (10) is true} \\ u^{4PCM}, & \text{otherwise} \end{cases}$$

$$v_{\max} = \begin{cases} v^{9PCM}, & \text{when Eq. (10) is true} \\ v^{4PCM}, & \text{otherwise} \end{cases} \quad (11)$$

The position (P, Q) of the singularity, in high precision, can be expressed as

$$P = p_{\max} + u_{\max},$$
$$Q = q_{\max} + v_{\max}. \quad (12)$$

3.3. Numerical Analysis of HCM

To verify the performance of HCM, we calculated the root mean square (RMS) and found the maximum error for the location of OV calculated by 9PCM, 4PCM and HCM, which is shown in Fig. 7. It is shown that the average error of HCM is not obviously reduced, comparing with 9PCM, as the region where 9PCM was replaced by 4PCM was limited in the corner of the distribution map. However, the maximum error of HCM was significantly lower than 9PCM, which showed that the error could be restrained in a low level.

A light beam was simulated to be transformed into an optical vortex beam, and emit on the SHWS. The signal of light beam was normalized, and added by a set of Gaussian white noise. The mean value of the noise was set 0, and the variance was set 0, 0.1, 0.2, 0.3, 0.4, 0.5. Through Fourier transform, the intensity on the CCD of SHWS can be calculated, and the phase slope data can be obtained. We calculated the RMS and found the maximum error for the location of OV calculated by 9PCM, 4PCM and HCM, as shown in Fig. 8. We could find out that the RMS of HCM was lower than the other two methods however big the Gaussian white noise is, and the peak of error of HCM retained low comparing with 9PCM. Overall, HCM showed robust performance.

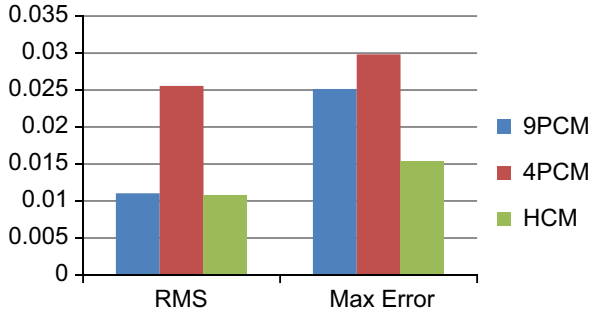

Fig. 7. The RMS and maximum error of 9PCM, 4PCM and MCM.

4. Experiment

In order to test our method, we built an experimental setup. A schematic of the setup is shown in Fig. 9. The LCOS-SLM used in our experiments was a phase-only modulation device (Hamamatsu Photonics, X10486-1) [20], which had 792×600 pixels with pixel sizes of $20\ \mu m \times 20\ \mu m$. The SHWS consisted of a lenslet array of pitch size $280\ \mu m$ and a high-speed intelligent vision sensor (Hamamatsu Photonics, H327) that had 512×512 pixels with pixel sizes of $20\ \mu m$ [21].

We confirmed the accuracy of detected positions by measuring the displacement of a singularity point with moving the location of the spiral phase pattern displayed on the LCOS-SLM. With steps of 1 pixel ($20\ \mu m$) in the LCOS-SLM plane, we made the movements along the horizontal direction. One pixel-length of the LCOS-SLM corresponded to 0.1142 in the u–v coordinate system at the SHWS plane, according to the parameters of our experimental system. We repeated experiments at different vertical positions on the LCOS-SLM and for different topological charges, and results are shown in Figs. 10–12. For simplicity, all of the measurements began with the center of the spiral phase pattern displayed at a pre-determined position near the center of the LCOS-SLM, and the pre-determined position was regarded as an initial position (0, 0), as shown in Figs. 10–12.

Fig. 10 shows an example of measured positions of horizontal component of singularity point versus the horizontal displacements of spiral phase pattern displayed on LCOS-SLM for topological charge $n=1$ by using the 9PCM, 4PCM, and HCM, where vertical positions (vp) was displaced 4 pixels from the initial vertical position. In the area near the center of lenslet (19.5 and 20.5), 4PCM showed lower error than 9PCM, and good linearity of HCM was shown after combining the two centroiding method.

We obtained the results at vertical positions (vp) -5, -3, 0, 2 and 4 pixels displaced from the initial vertical position for different topological charges and are shown in Fig. 11(a) $n=1$, (b) $n=2$, and (c) $n=3$. The averages of the measurements are shown in Fig. 11(d). The two vertical dashed lines in Fig. 11(a) indicate the range that corresponds to a displacement equal to the lens size of the lenslet array, and the diagonal line from bottom-left to top-right is a theoretical prediction. The results show good linearity between the measured position of the singularity point and the displacement applied by the LCOS-SLM. The slope of the line

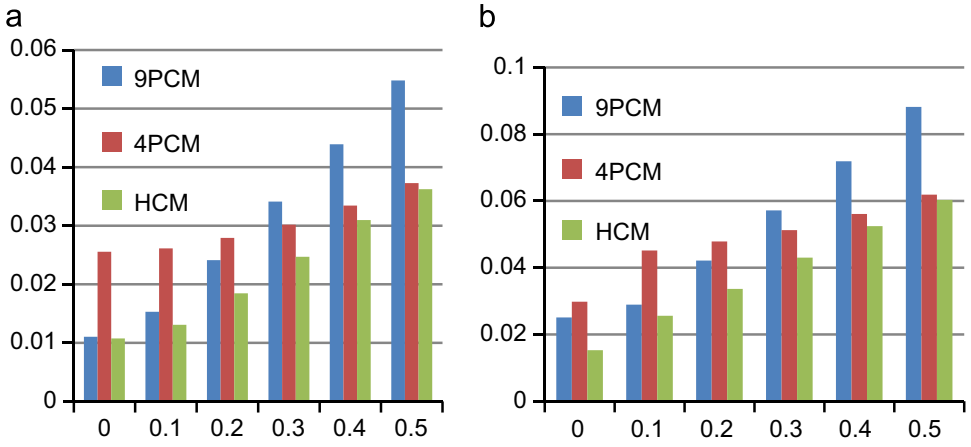

Fig. 8. The RMS (a) and maximum error (b) of 9PCM, 4PCM and MCM, when the variance of Gaussian white noise was 0, 0.1, 0.2, 0.3, 0.4 and 0.5.

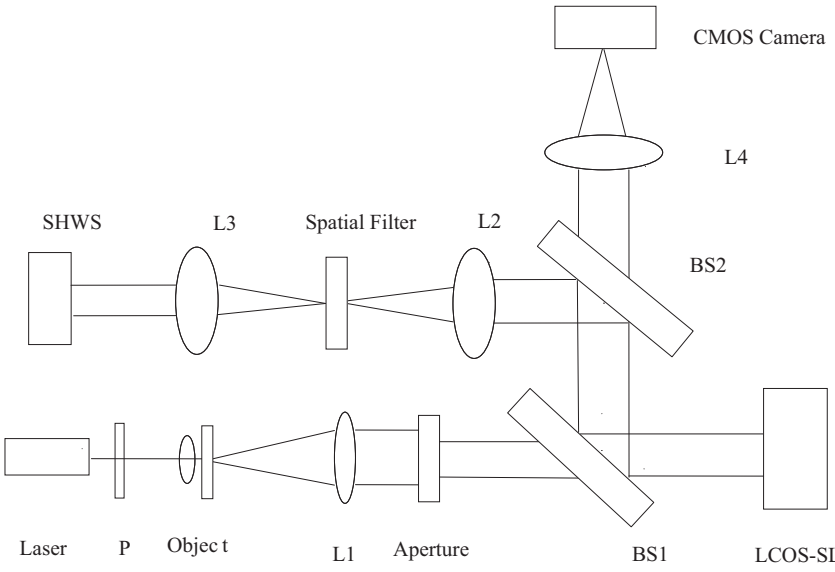

Fig. 9. Optical setup. P: Polarizer; BS1, BS2: Beam splitter; L1, L2, L3, L4: Lens; SLM: Spatial light modulator; SHWS: Shack–Hartmann wavefront sensor.

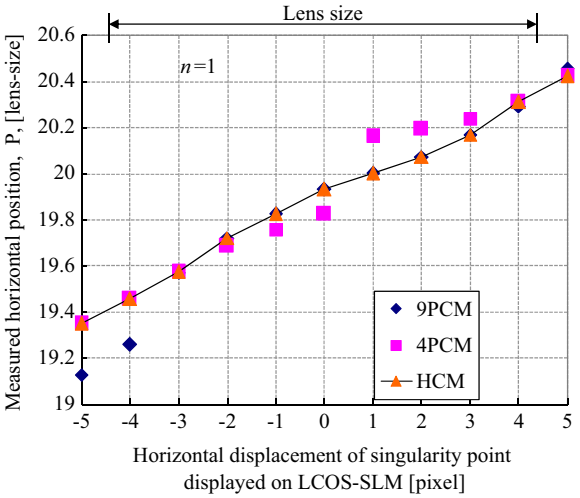

Fig. 10. Plots of measured positions of horizontal component of singularity point versus the horizontal displacements of spiral phase pattern displayed on LCOS-SLM for topological charge $n=1$ by using the 9PCM, 4PCM, and HCM.

fitting those measured horizontal positions is 0.1127, which agrees well with the theoretically predicted value 0.1142. The average root mean square (RMS) error over various measurements was approximately 0.044, in unit of normalized lenslet size.

We measured the vertical components when the vortex point on the LCOS-SLM was displaced along the horizontal direction for different topological charges and are shown in Fig. 12(a) $n=1$, (b) $n=2$, and (c) $n=3$. Fig. 12(d) plots the vertical component of the measured position versus the displacement in the vertical direction.

The RMS error of the horizontal and vertical components is 0.044 and 0.052, and its averaged value over the measurements for the horizontal and vertical components is 0.048. It means that the precision is approximately one-twentieth of the lens size of the lenslet array. The RMS of 9PCM, 4PCM, HCM, CMM for the topological charge $n=1$, 2, 3 is shown in Table 1. It is indicated that HCM showed advantage over 9PCM and 4PCM, which linked to the results of the numerical simulations that were presented. Also, the performance of HCM is not worse than that of CMM [18], the method we proposed before.

There are several different sources of uncertainty and error in the optical system, containing finite pixelization, cross-talk between lenslets, out-of-range conditions, background light, spot motion during the exposure time, light incident during the CCD readout, and several other effects. One of the major factors that affect the detection accuracy is the zero-amplitude characteristic of the singularity point in an optical vortex beam. As shown in Fig. 13, a dark area around the point could be observed in the Hartmanngram even though it was recorded at the conjugate plane of the LCOS-SLM where the spiral phase pattern was displayed. Within this area, the spots of the Hartmanngram may be deformed, and in the worst case, one or more spots will disappear. Therefore, as shown in Figs. 11 and 12, the measurement error may vary according to the positional relationship between a vortex point and the lenslets. Also, the artifact noise caused by 2π-phase-wrapping lines in the pattern displayed on LCOS-SLM might increase the measurement error, especially when the detected vortex was of large topological charge and near to the contour of integration. The method we proposed, however, has shown high accuracy and robust performance.

The implementation time for HCM is less than 1 ms in a common personal computer (CPU: Intel Core2 2.0 GHz; RAM: 1 GB). It is much faster than that of CMM, the average time of which is more than 70 ms.

5. Summary

In summary, a new hybrid centroiding framework has been proposed to realize high-spatial-resolution detection of the positions of singularity points in optical vortex beam using a Shack–Hartmann wavefront sensor (SHWS). We first determined the singularity's position precisely by 9PCM, which calculated the centroid of the circulation of 3×3 crosspoints. After that, we analyzed the error distribution of 9PCM, and proposed hybrid centroiding framework, which combines two centroiding methods. Numerical calculation showed that the new framework improved the accuracy of detection the position of OV. Good linearity was also verified between the measured position shifts of the singularity point and the displacements of the spiral phase position. The average root mean square (RMS) error over various measurements was better than CMM, the method we proposed

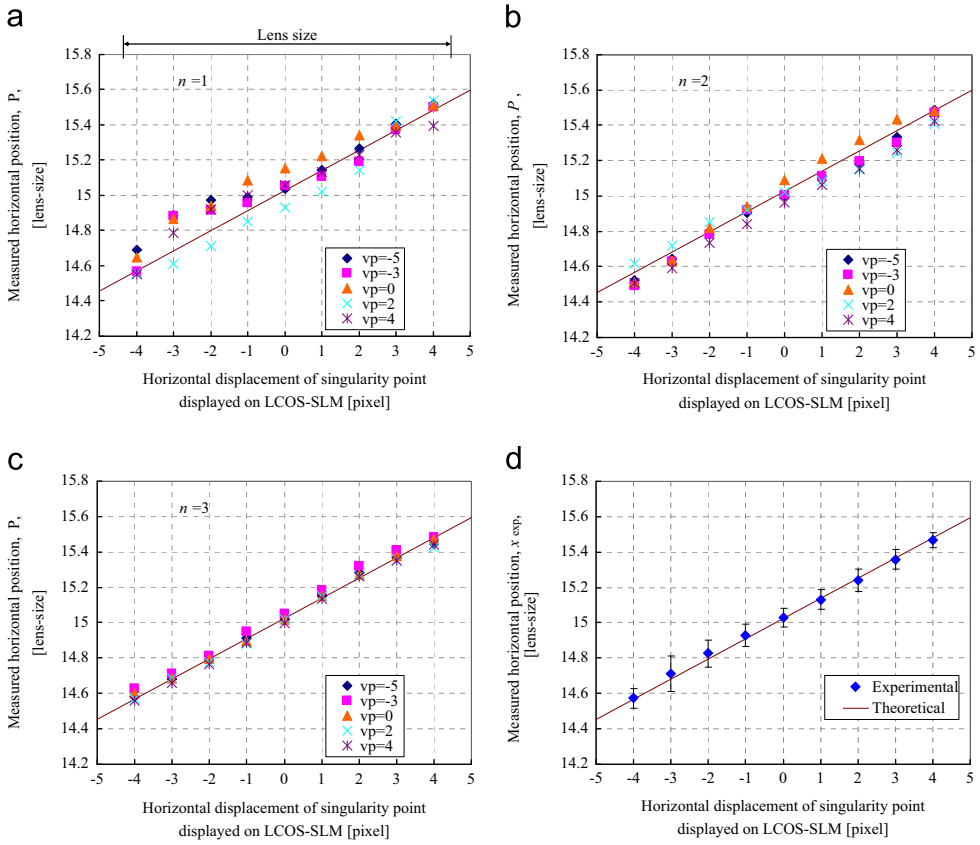

Fig. 11. Plots of measured positions of horizontal component of singularity points versus the horizontal displacements of spiral phase pattern displayed on LCOS-SLM for topological charge (a) $n=1$, (b) $n=2$, and (c) $n=3$, and plot of averages of horizontal component measured versus the horizontal displacements assigned (d).

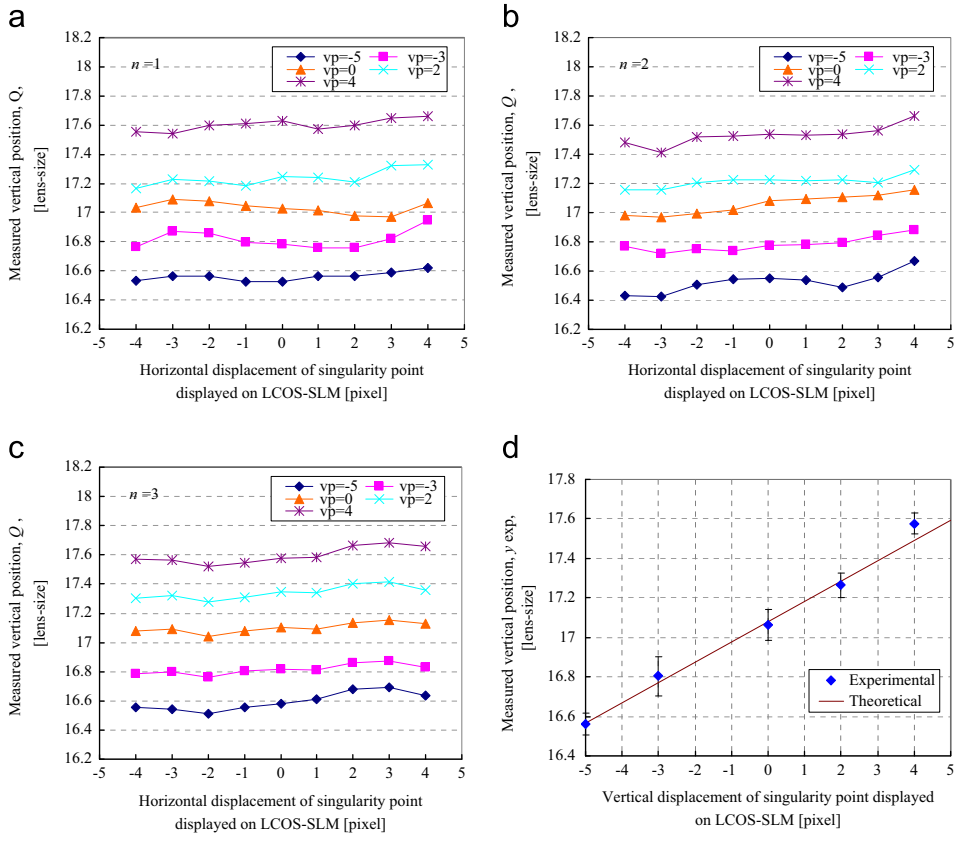

Fig. 12. Plots of measured positions of vertical components of singularity point versus the horizontal displacements of spiral phase pattern for topological charge (a) $n=1$, (b) $n=2$, and (c) $n=3$, and plot of the averages of vertical component measured versus the vertical displacements assigned (d).

Table 1
The RMS of 9PCM, 4PCM, HCM, CMM for the topological charge $n=1$, 2 and 3.

	9PCM	4PCM	HCM	CMM
$n=1$	0.071	0.082	0.061	0.058
$n=2$	0.058	0.065	0.047	0.042
$n=3$	0.044	0.054	0.036	0.064
Average	0.058	0.067	0.048	0.055

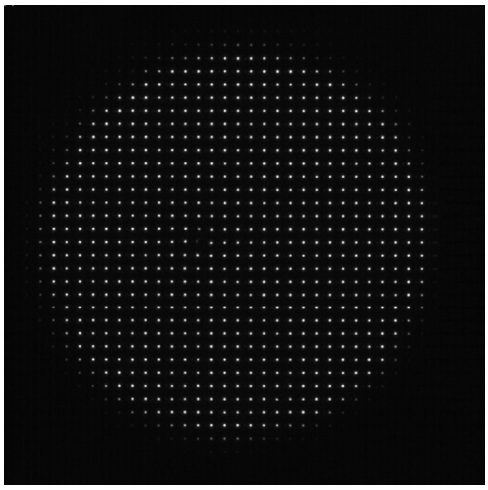

Fig. 13. An example of Hartmanngram.

before. The method showed higher accuracy and the implementation time was significantly reduced comparing with our former work.

Acknowledgments

The authors are grateful to A. Hiruma and T. Hara for their support and encouragement throughout this work, and to N. Matsumoto and Y. Takiguchi for useful discussions. This work was supported in part by the National Basic Research Program (2010CB732504), the Natural Science Foundation of Zhejiang (R12F030004), and the National Natural Science Foundation of China (61271083).

References

[1] J.F. Nye, M.V. Berry, Proceedings of the Royal Society of London Series A 336 (1974) 165–190.
[2] D.L. Fried, J.L. Vaughn, Applied Optics 31 (15) (1992) 2865–2882.
[3] L. Bigot, W.J. Wild, E.J. Kibblewhite, Proceedings of SPIE 3381 (1998) 76–86.
[4] D.L. Fried, Journal of the Optical Society of America A 15 (10) (1998) 2759–2768.
[5] J. Wu, H. Li, Y. Li, Optical Engineering 46 (1) (2007) 019701.
[6] J.E. Curtis, B.A. Koss, D.G. Grier, Optics Communications 207 (1–6) (2002) 169–175.
[7] E. Auksorius, B.R. Boruah, C. Dunsby, P.M.P. Lanigan, G. Kennedy, M.A.A. Neil, P.M.W. French, Optics Letters 33 (2008) 113–115.
[8] W. Wang, Y. Qiao, R. Ishijima, T. Yokozeki, D. Honda, A. Matsuda, S.G. Hanson, M. Takeda, Optics Express 16 (18) (2008) 13908–13917.
[9] F.A. Starikov, G.G. Kochemasov, S.M. Kulikov, A.N. Manachinskv, N.V. Maslov, A.V. Ogorodnikov, S.A. Sukharev, V.P. Aksenov, I.V. Izmailov, F.Y. Kanev, V.V. Atuchin, I.S. Soldatenkov, Optics Letters 32 (16) (2007) 2291–2293.
[10] C. Rockstuhl, A.A. Ivanovskyy, M.S. Soskin, M.G. Salt, H.P. Herzig, R. Dandliker, Optics Communications 242 (2004) 163–169.
[11] N. Matsumoto, T. Ando, T. Inoue, Y. Ohtake, N. Fukuchi, T. Hara, Journal of the Optical Society of America A 25 (7) (2008) 1642–1651.
[12] D.R. Neal, J. Copland, D. Neal, Proceedings of SPIE, 4779, 148–160.
[13] A. Chernysgov, U. Sterr, F. Riehle, J. Helmcke, J. Pfund, Applied Optics 44 (30) (2005) 6419–6425.
[14] F.A. Starikov, V.P. Aksenov, V.V. Atuchin, I.V. Izmailov, F.Y. Kanev, G.G. Kochemasov, A.V. Kudryashov, S.M. Kulikov, Y.I. Malakhov, A.N. Manachinsky, N.V. Maslov, A.V. Ogorodnikov, I.S. Soldatenkov, S.A. Sukharev, Proceedings of SPIE 6747 (67470P) (2007) 18.
[15] F.A. Starikov, V.P. Aksenov, V.V. Atuchin, I.V. Izmailov, F.Y. Kanev, G.G. Kochemasov, S.M. Kulikov, A.N. Manachinsky, N.V. Maslov, A.V. Ogorodnikov, I.S. Soldatenkov, S.A. Sukharev, Proceedings of SPIE 7131 (7131G-1) (2009) 1–7.
[16] K. Murphy, D. Burke, N. Devaney, C. Dainty, Optics Express 18 (15) (2010) 15448–15460.
[17] K. Murphy, C. Dainty, Optics Express 20 (5) (2012) 4988–5002.
[18] C. Huang, H. Huang, H. Toyoda, T. Inoue, H. Liu, Optics Express 20 (24) (2012) 26099–26109.
[19] M. Chen, F.S. Roux, J.C. Olivier, Journal of the Optical Society of America A 24 (7) (2007) 1994–2002.
[20] T. Inoue, H. Tanaka, N. Fukuchi, M. Takumi, N. Matsumoto, T. Hara, N. Yoshida, Y. Igasaki, Y. Kobayashi, Proceedings of SPIE 6487 (2007) 64870Y.
[21] H. Huang, T. Inoue, T. Hara, Proceedings of SPIE 7156 (2008) 71560F.